Energy Technology
Generation, Conversion, Storage, Distribution
www.entechnol.de

Fabrication of Flexible Supercapacitor Using Spray-Coated $Ti_3C_2T_x$ MXene Thin Film

Varsha Vijayan, Anamika Ashok, Asha Arackal Sukumaran, Oleksii Klymov, Carmen Martinez-Tomas, Said Agouram, Vicente Muñoz-Sanjose, Mahesh Eledath Changarath, and Juan F. Sánchez Royo*

Fabrication of a flexible symmetric supercapacitor with an areal capacitance of 28.40 mF cm^{-2} using spray-coated $Ti_3C_2T_x$ MXene thin film is reported here. $Ti_3C_2T_x$ MXene thin films are successfully deposited by a spray coating method on a flexible polymer substrate. The thin films exhibit a significant d spacing of 1.54 nm, and the conductivity of the films increases with spray time up to a maximum of 2.32 × 10^4 S m^{-1} giving an areal capacitance of 62.15 mF cm^{-2} at a 5 mV s^{-1} scan rate. The thin film shows capacitive character with 93% of its total charge from capacitive contribution, at a scan rate of 100 mV s^{-1}. The structural and morphological analysis confirms the formation of large $Ti_3C_2T_x$ flakes, contributing to enhanced conductivity and electrochemical response. An all-solid-state symmetric supercapacitor developed using the optimized thin films as the electrodes and PVA-H_2SO_4 gel polymer as the electrolyte gives an energy density of 2.52 μWh cm^{-2} and a power density of 105.20 μW cm^{-2} at a current density of 1 mA cm^{-2}.

1. Introduction

The rapid advancement of consumer electronics, particularly smartphones and wearable devices, has driven the development of high-performance energy storage solutions.[1] Compared to batteries, supercapacitors have emerged as a promising candidate due to their unique advantages, such as fast charge/discharge capabilities, high power densities, and ultra-long cycle life[2] making them attractive for integration into modern electronic devices, particularly wearable devices.[3,4] The development of flexible supercapacitors with improved energy density, high power density, and cycle life is crucial for the seamless operation of wearable devices.[5] New electrode materials, electrolytes, and device architectures are being investigated to accomplish this objective.[6] Multicomponent and heterostructured electrode materials—including LDH-based nanoarrays,[7] MXene-C_3N_5 hybrid systems,[8] Z-scheme heterostructures,[9] dual-metal hydroxide frameworks,[10] biomass-derived hierarchical porous carbons,[11,12] and MOF-based systems[13]—have demonstrated promising pathways to synergistically enhance redox activity, charge transport, and structural integrity in high-performance supercapacitors.[14,15]

Recent supercapacitor research focuses on developing pseudocapacitive electrode materials,[16] which provide large specific capacitance, facilitated by fast surface redox reactions, compared to electric double-layer capacitor (EDLC) materials.[17,18,19,20] Common challenges encountered in pseudocapacitive materials, such as limited electrical conductivity,[21,22] high production costs,[23] and structural instability during ion extraction and insertion, hinder their practical applications.[24,25] Therefore, there is an urgent need to develop new supercapacitor electrode materials that are cost-effective, offer high power and energy density, and exhibit excellent cycling stability. The integration of transition metal oxides like NiO and Co_3O_4 with a TiO_2 matrix has demonstrated synergistic enhancement of redox activity and structural integrity, enabling high capacitance and prolonged cycling stability in supercapacitor electrodes.[26] The synergistic combination of

V. Vijayan, A. Ashok, A. Arackal Sukumaran
Nanomaterials for Emerging Solid-state Technology (NEST) Research Laboratory
Department of Physics
Cochin University of Science and Technology
Kochi 682022, India
E-mail: asa@cusat.ac.in

A. Arackal Sukumaran
Centre of Excellence in Advanced Materials
Cochin University of Science and Technology
Kochi 682022, India

The ORCID identification number(s) for the author(s) of this article can be found under https://doi.org/10.1002/ente.202500317.

DOI: 10.1002/ente.202500317

A. Arackal Sukumaran
Inter University Centre for Nanomaterials and Devices (IUCND)
Cochin University of Science and Technology
Kochi 682022, India

O. Klymov, C. Martinez-Tomas, S. Agouram, V. Muñoz-Sanjose
Department of Applied Physics and Electromagnetism
University of Valencia
c/ Dr. Moliner nº 50, Burjassot 46100, Spain

M. Eledath Changarath, J. F. Sánchez Royo
Institute of Materials Science (ICMUV)
University of Valencia
c/ Catedrático José Beltrán, Paterna 46980, Spain

MoS_2 and MXene enhances ion transport and faradaic activity, resulting in improved capacitance and cycling stability for flexible supercapacitor devices.[27] MXene-based MnO_2 nanocomposites have demonstrated outstanding electrochemical performance with specific capacitance as high as 457 $F g^{-1}$ and excellent cycling efficiency (102.5% after 1000 cycles), attributed to the synergistic interaction between MXene and MnO_2.[28] Electrolytes significantly influence both energy density and safety, with aqueous, organic, and ionic liquid electrolytes being widely used despite challenges like leakage, electrode shorting, and corrosion.[29,30] MXenes exhibit excellent cycling stability in acidic aqueous electrolytes due to fast proton intercalation, while their performance in alkaline media is generally lower owing to limited ion accessibility and higher oxidation susceptibility.[31] Emerging electrolytes such as deep eutectic solvents, ionic liquids, and organic systems offer wider electrochemical windows and enhanced energy densities, though often at the expense of reduced rate capability and cycling stability due to sluggish ion diffusion.[32] Even though aqueous electrolytes have fast ion transport contributing to excellent power performance, the narrow electrochemical stability window (1.23 V) limits the energy density of the devices[33] developed using them. Solid or quasi-solid electrolytes are being investigated to enhance safety and performance.[29] Gel polymer electrolytes (GPEs), which are quasi-solid-state electrolytes, offer higher ionic conductivity and flexibility compared to solid polymer electrolytes.[34] Among the various GPEs, poly(vinyl alcohol) (PVA) stands out for its hydrophilicity, nontoxicity, low cost, and suitability for flexible supercapacitor designs.[35,36]

$Ti_3C_2T_x$ a member of 2D transition metal carbides/nitrides, MXenes,[37] with its pseudocapacitive nature, rendered by the rich surface functional groups,[38] together with high volumetric capacitance due to the large interlayer spacing,[39] high conductivity due to the presence of metallic Ti,[40] large specific surface due to its 2D morphology,[41] is an exceptional candidate for supercapacitor electrode. The high Young's modulus[42] provides the material with excellent flexibility, to withstand mechanical deformations such as folding,[43] twisting, and bending,[44] making it a suitable candidate for fabricating wearable supercapacitors, capable of withstanding stresses and strains associated with body movements.[45,46] $Ti_3C_2T_x$ MXene possesses a rich surface chemistry, with functional terminations such as –OH, –F, and –O introduced during the etching process. These groups influence several aspects of electrochemical behavior: Surface terminations, particularly –OH and –O, can enhance pseudocapacitive behavior through redox reactions.[31] However, an excess of –F terminations, which are electrochemically inactive, may reduce capacitance.[47] Careful control of surface chemistry is thus essential to improve energy storage performance. The hydrophilic nature of the surface functional groups facilitates interaction with the electrolyte.[48] However, in solid-state configurations, the limited fluidity of the electrolyte restricts access to these active sites, thereby lowering effective capacitance.[49] Delamination improves interlayer spacing and increases accessible surface area, but incomplete exfoliation or partial restacking during film fabrication can limit these advantages.[50] Zhou et al. fabricated an MXene/reduced graphene oxide (RGO) composite film using vacuum-assisted filtration (VAF), achieving an areal capacitance of 49 $mF cm^{-2}$.[51] Incorporating biocompatible and mechanically robust polymers such as cellulose into MXene-based composites has been shown to improve the structural integrity and flexibility of supercapacitor electrodes, without compromising electrochemical performance.[52] However, these freestanding films were brittle, which affected their durability and long-term cycling stability. Wearable device technology, therefore, looks for thin film supercapacitors developed on flexible substrates, which facilitates easy integration with wearable sensors.[53] Thin film electrodes can also eliminate the need for additional conductive additives and binders, typically required when electrode materials are coated onto the current collectors.[54] This approach has been demonstrated using free-standing MXene films that show excellent electrochemical performance without the use of such additives.[31]

The chemical vapor deposition technique has been utilized to create diverse MXene thin films on various substrates.[55] However, the elevated production expenses and restrictions in scale pose challenges for commercial applications. Moreover, spin coating[56] and electrodeposition methods[57] have shown high equivalent series resistance values because of the large inter-flake distance. Even though thin film fabrication by sputtering yields films with good adhesion and uniformity, the high cost and the elaborate steps in thin film deposition prohibit scalability.[58] Blade coating[59] offers simplicity and scalability but struggles with achieving uniform film thickness, especially over large areas, and often results in poor surface smoothness. The spray-coating technique has emerged as an innovative solution-based approach for creating MXene films made up of large flakes to address these challenges.[60] It is one of the quickest approaches for producing thin films. Compared to the spin-coating technique, the easy regulation of the deposition parameters, such as spray flow, spray speed, substrate characteristics, and the number of spray cycles to control the thickness and properties of the thin film and the ability to cover complex geometries uniformly, makes the technique scalable.[61] Gogotsi et al. manufactured Ti_3C_2 MXene thin films with thicknesses ranging from 5 to 70 nm by employing the spray-coating technique for electrochromic application.[62] Tomov et al. demonstrated the successful fabrication of spray-coated $Ti_3C_2T_x$ MXene thin films for biosensor applications, highlighting their uniform surface coverage and excellent electrical conductivity.[60] Similarly, Hantanasirisakul et al. fabricated transparent and conductive $Ti_3C_2T_x$ thin films with tunable optoelectronic properties using a spray-coating technique, showcasing the method's potential for scalable thin-film electronics.[62] These examples support the broader relevance and adaptability of MXene thin films for various applications, including energy storage, electrochromics, and sensing technologies. $Ti_3C_2T_x$ thin films produced via electrohydrodynamic atomization (EHA)[63] suffer from nonuniform thickness and lower conductivity due to the challenges in controlling droplet size and maintaining uniform deposition. Therefore, there is an urgent requirement to develop uniform thin films through scalable routes that enable precise control of the film properties by controlling the deposition parameters.

We report a scalable and controllable spray coating technique for fabricating flexible $Ti_3C_2T_x$ MXene thin films tailored for energy storage applications. This approach offers precise regulation of film thickness and flake size, which is critical for optimizing electrochemical performance. Notably, the use

of spray-coated $Ti_3C_2T_x$ MXene thin films as flexible supercapacitor electrodes has not been previously reported, marking a significant advancement in MXene processing methods. The spray time is varied to fabricate conducting thin films on a flexible substrate. An evaluation of the variation of electrochemical properties of the thin film with spray duration is carried out in the study. Optimization of the concentration of H_2SO_4 is done to obtain PVA-H_2SO_4 GPE with good ionic conductivity. A symmetric all-solid-state flexible supercapacitor is fabricated using the optimized thin film and GPE to give an areal capacitance of 28.40 mF cm^{-2}, an energy density of 2.52 μWh cm^{-2}, and a power density of 105.20 μW cm^{-2} at a current density of 1 mA cm^{-2}. The study also proposes a mechanism of electron transport to evaluate the enhancement in electrochemical performance with spray time, the first of this kind, adding novelty to the work.

2. Experimental Section

2.1. $Ti_3C_2T_x$ MXene Thin Films by Spray Coating

The $Ti_3C_2T_x$ MXene was synthesized from commercially obtained Ti_3AlC_2 MAX phase (titanium aluminum carbide 312, ≥90%, particle size ≤40 μm, purchased from Sigma–Aldrich) using an in situ HF forming etching technique using LiF and HCl.[64] 0.5 g of the resulting $Ti_3C_2T_x$ MXene powder was dispersed in 100 mL of deionized water and subjected to sonication for 1 h to obtain a uniform dispersion. Subsequently, the dispersion was centrifuged at 2500 rpm for 1 h, and the supernatant was collected for spray coating the thin films. The films were spray-coated onto substrates using air as the carrier gas. The spray coating process was carried out by varying the spray time (10–60 min) on fluorine-doped tin oxide (FTO)-coated glass substrates,flexible polymer substrates and carbon cloth (CC). The substrate temperature was maintained at 100 °C, with a spray pressure set at 0.25 bar. A schematic illustration of the preparation of $Ti_3C_2T_x$ MXene powder and the subsequent fabrication of a thin film is shown in **Figure 1**.

2.2. Characterization Techniques

X-ray diffraction (XRD) patterns of $Ti_3C_2T_x$ MXene powder were obtained with a Rigaku MiniFlex X-ray diffractometer, utilizing the CuKα radiation (λ = 1.54 Å). Bruker D8 ADVANCE A25 XRD system was used to analyze the crystalline phases of thin films. Further, HRXRD of the thin film at 2θ-ω configuration were carried out using a Panalytical X-Pert MRD diffractometer. Raman spectroscopy was done using a HORIBA MTB. XPlora spectrometer equipped with 532 and 785 nm lasers. A scanning electron microscope (SEM), HITACHI S4800 equipped with an X-ray detector, was employed to examine the morphology. Transmission electron microscopy (TEM) was performed using a HRTEM TECNAI 200 kV field emission gun (FEG) with a resolution (Point Resolution) of 0.24 nm. UV-vis spectra were recorded with a Varian Cary 4000 spectrophotometer. The sheet resistance of the films was measured using a four-point probe instrument (Ossila Four Point Probe Test System). XPS measurements were performed in a SPECS GmbH system (base pressure 1×10^{-10} mbar) equipped with an ASTRAIOS 190 2D-CMOS hemispherical analyzer. For the XPS measurements, photoelectrons were excited with the Al K_α line (1486.7 eV) of a monochromatic X-ray source [μFOCUS 500 (SPECS GmbH)]. Electrochemical measurements were performed using the electrochemical workstation CHI-6054E. $Ti_3C_2T_x$ thin film with ≈1 cm^2 active area on the polymer substrate, platinum mesh with ≈1 cm^2 surface area, Ag/AgCl in 3 M KCl, and 3 M H_2SO_4 were used as a working electrode (WE), counter electrode (CE), reference electrode (RE), and electrolyte, respectively. **Figure 2**a shows

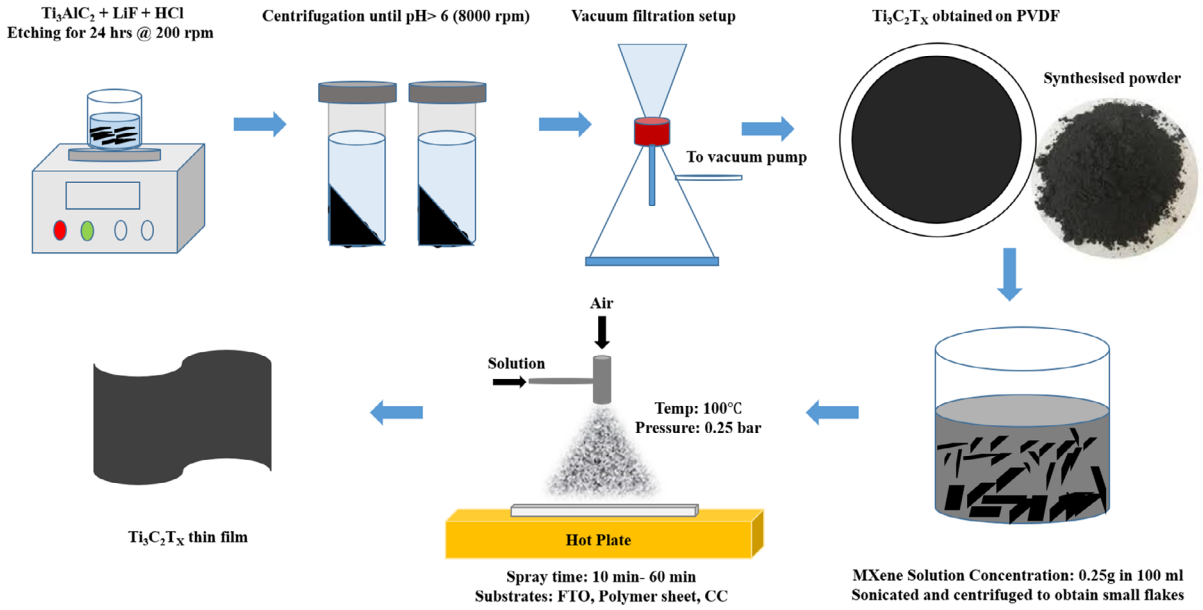

Figure 1. Schematic illustration of synthesis of $Ti_3C_2T_x$ MXene powder from Ti_3AlC_2 MAX phase and the fabrication of thin film by spray coating technique.

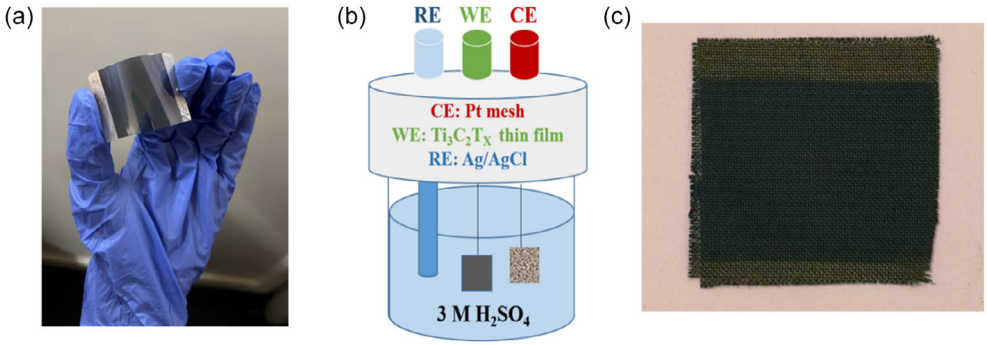

Figure 2. a) Photograph of $Ti_3C_2T_x$ MXene thin film coated for 60 min on polymer substrate at a substrate temperature of 100 °C. b) Schematic illustration of the three-electrode setup configuration used for electrochemical characterization in the study. c) Photograph of $Ti_3C_2T_x$ MXene thin film coated for 60 min on CC at a substrate temperature of 100 °C.

the photograph of $Ti_3C_2T_x$ MXene thin film synthesized for 60 min at a substrate temperature of 100 °C, and Figure 2b shows the schematic of the three-electrode setup used for electrochemical characterization in the study and Figure 2c shows the photograph of $Ti_3C_2T_x$ MXene thin film coated for 60 min on CC at a substrate temperature of 100 °C.

2.3. Synthesis of PVA-H_2SO_4 Gel Polymer Electrolyte

One gram of polyvinyl alcohol (PVA) is dissolved in 10 mL of dilute H_2SO_4 under continuous stirring at a temperature of 80 °C for 2 h to form a clear, homogeneous gel. The concentration of H_2SO_4 has been varied to optimize the ionic conductivity of the electrolyte. The gel is then poured into a petri dish and allowed to cool and cure, ensuring structural stability and uniformity. The ionic conductivity of the GPE was determined from impedance spectroscopy studies conducted using HP 4192A impedance analyzer, and the value is calculated using the equation

$$\sigma = \frac{d}{R_b A} \tag{1}$$

where d is the thickness of the GPE film, R_b is the bulk resistance which can be obtained from the electrochemical impedance spectra (EIS), and A is the area of the film.[35]

2.4. Symmetric Supercapacitor Device Characterization

A symmetric supercapacitor device was assembled using in a Swagelok cell. The electrodes were spray-coated $Ti_3C_2T_x$ MXene thin film on CC, with 0.5 M PVA-H_2SO_4 GPE serving as the separator. The areal capacitance, energy density, and power density were determined using the following equations

$$\text{Areal capacitance, } C_A = \frac{I\Delta t}{A\Delta V} \tag{2}$$

$$\text{Energy density, } E = \frac{C_A(\Delta V)^2}{7200} \tag{3}$$

$$\text{Power density, } P = \frac{E}{\Delta t} \tag{4}$$

where I is the current (A), ΔV is the potential window (Volt), A is the active electrode area (cm^2), and Δt is discharging time in hours.

3. Results and Discussions

A comparison of the XRD patterns of Ti_3AlC_2 MAX phase and $Ti_3C_2T_x$ MXene powder given in **Figure 3**a confirm the successful mild etching of the Ti_3AlC_2 MAX phase. The (002) peak of the MAX phase appears at a 2θ angle of 9.6°, corresponding to a d-spacing of 0.92 nm. The (002) peak of MXene occurs at a lower 2θ value of 6.2°, indicating an increase in the d-spacing to 1.4 nm, suggesting the removal of Al layers.[65] Further, a reduction in the intensity of the (104) peak associated with the Ti—Al bond in the $Ti_3C_2T_x$ MXene powder suggests partial etching of the MAX phase.[66] Figure S1 in the Supporting Information gives the FESEM and HRTEM images of the synthesized MXene powder. The layered morphology of MXene is clearly revealed in the FESEM image, and the HRTEM confirms the d spacing corresponding to the planes obtained from the XRD. The interlayer spacing in $Ti_3C_2T_x$ MXene plays a crucial role in determining its electrochemical properties, as large interlayer spacing can facilitate more ion intercalation, enhancing the electrochemical performance of the material.[39] However, this increased spacing can also have a downside. The overlap between the Ti and C orbitals in the MXene decreases as the layers move further apart. This reduced overlap can lead to a drop in electrical conductivity because the electronic pathways within the material are disrupted.[67]

Figure 3b shows the XRD pattern of MXene thin films deposited on the polymer substrates at different spray times. It can be seen that the $Ti_3C_2T_x$ thin films present a preferential orientation along the (002) direction and the intensity of this diffraction peak increases with spray time. The emergence of the (002) peak at a 2θ value of 5.74° suggests a further increase in d-spacing to 1.54 nm, resulting from the additional sonication of the MXene colloid before spray coating. In order to clearly separate the peaks of the MXene thin film from those of the substrate, 2θ scans at a grazing incidence of 3 degrees were obtained. **Figure 4** shows the diffraction patterns at both conventional and grazing incidence for the thin film grown at 100 °C for 60 min. At grazing

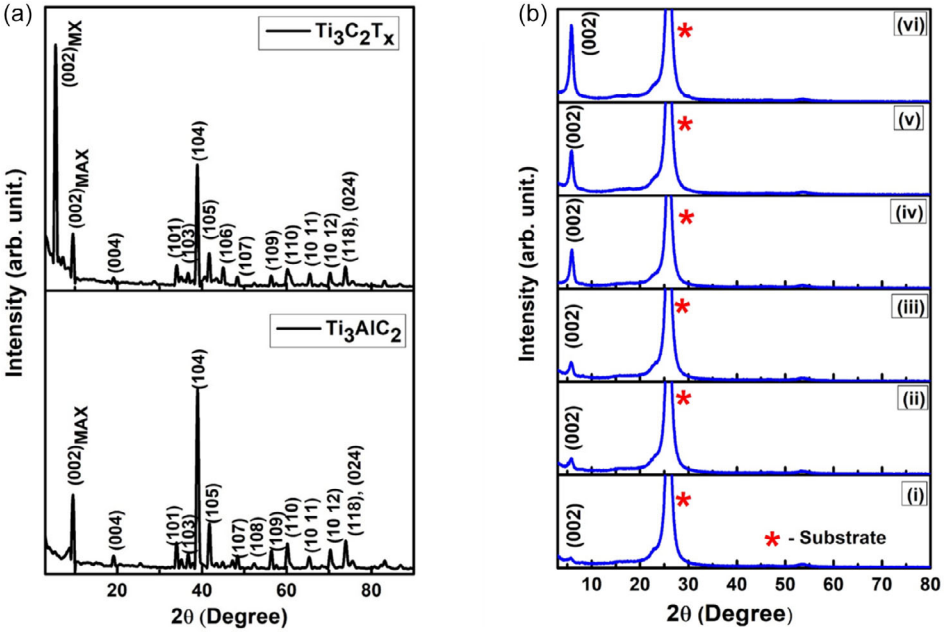

Figure 3. Comparison of XRD pattern of a) Ti_3AlC_2 MAX phase and $Ti_3C_2T_x$ MXene powder and b) $Ti_3C_2T_x$ MXene thin films deposited on polymer substrates at different spray times (i) 10 min, (ii) 20 min, (iii) 30 min, (iv) 40 min, (v) 50 min, and (vi) 60 min.

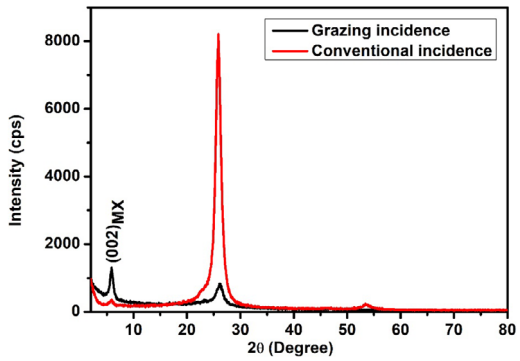

Figure 4. XRD pattern of $Ti_3C_2T_x$ MXene thin films grown at 100 °C on a polymer substrate for a spray time of 60 min, using conventional and grazing incidence.

incidence, the (002) reflection from the film increased its intensity, while that from the substrate reduced its intensity, confirming undoubtedly the provenance of peaks. The increasing trend in the intensity of the (002) peak was further confirmed by simultaneously spray coating $Ti_3C_2T_x$ MXene thin films on FTO-coated glass substrate, the XRD pattern of which (Figure S2a in Supporting Information) showed a similar trend. The enhancement of the intensity of (002) plane reflection may be due to the better alignment and stacking of the flakes in the coating process, making the $Ti_3C_2T_x$ MXene flake more uniform and possibly larger.

The argument is supported by the FESEM image (**Figure 5**), which shows the evolution of morphology of the thin film with spray time. The small grains at low spray time have coalesced to form large flakes, reducing the inter-flake junctions. The cross-sectional SEM image of **Figure 6**a and Figure S3 (Supporting Information) reveals a layered morphology with the MXene flakes arranged in distinct layers to form a thin film. The average thickness of the $Ti_3C_2T_x$ MXene thin film spray coated for 60 min on FTO-coated glass substrate is 863 nm. The TEM image (Figure 6b) further reveals the flake like morphology with the high-resolution transmission electron microscopy (HRTEM) image, Figure 6c, indicating the layered structure of layered structure of $Ti_3C_2T_x$ MXene, specifically highlighting the (002) plane, with a d spacing of 1.54 nm confirming the XRD results.

The lattice c-parameter is determined using the plane spacing equation for a hexagonal crystal structure

$$\frac{1}{d^2} = \frac{4}{3}\left(\frac{h^2 + hk + k^2}{a^2}\right) + \frac{l^2}{c^2} \quad (5)$$

Here, the "*d*" refers to the interplanar spacing; *h*, *k*, and *l* refer to the Miller indices of the planes; and "*a*" and "*c*" are the lattice parameters. The c-lattice parameter increased from 28.51 Å in the $Ti_3C_2T_x$ MXene powder to 30.79 Å in the $Ti_3C_2T_x$ thin film, further indicating an increase in interlayer spacing. The selected area diffraction pattern (Figure 6d) indicates that the thin film is of a polycrystalline nature, consistent with the hexagonal lattice. Energy-dispersive X-ray spectroscopy (EDAX) (Figure S4 in Supporting Information) of the thin film indicated the thin film to be composed of Ti, C, O, and F, with little or no Al, indicating the success of etching and the substitution of the Al layers with O/OH and/or F functional groups.[65]

Figure 7 reveals the distinct vibrational Raman modes, characteristic of $Ti_3C_2T_x$ MXene, obtained on a thin film coated on a polymer substrate using an excitation of 532 nm and 785 nm. The thin film deposited on FTO-coated glass substrate also gave

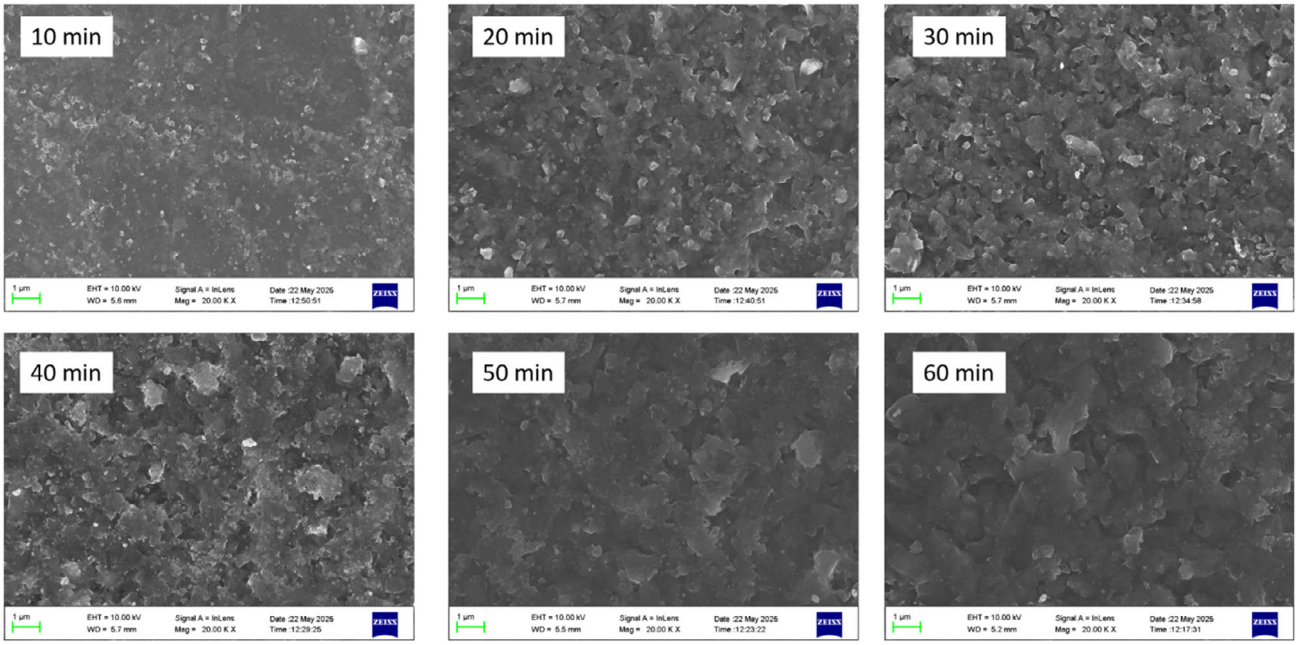

Figure 5. FESEM image of $Ti_3C_2T_x$ MXene thin films spray coated for different spray times on polymer substrate.

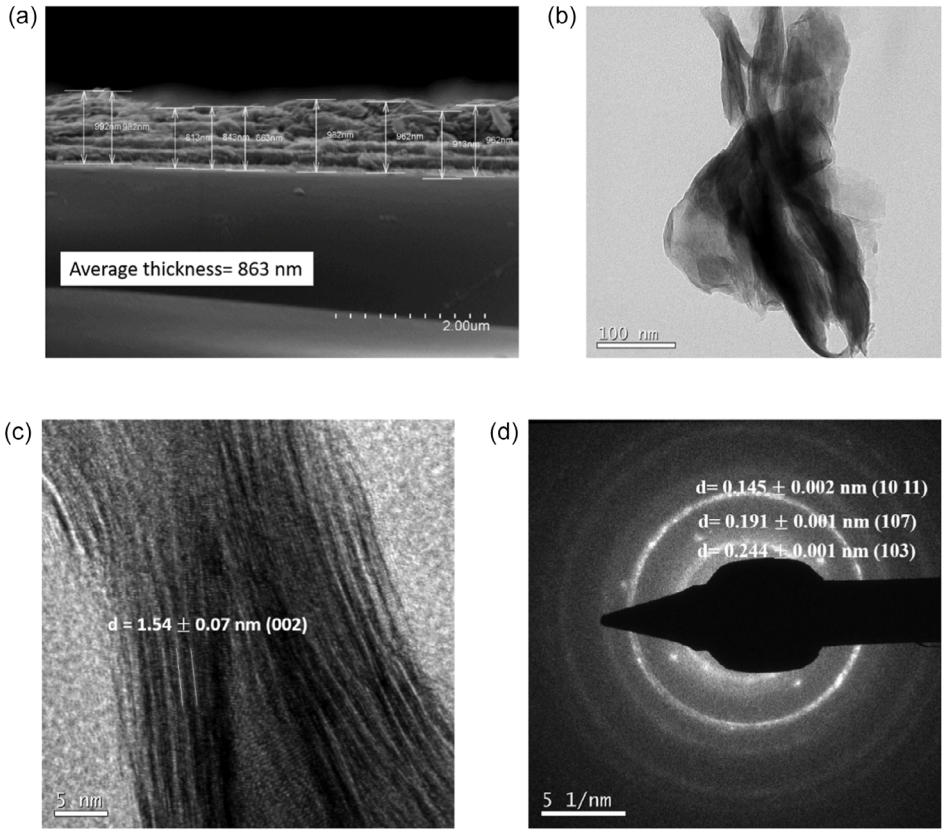

Figure 6. a) Cross-sectional SEM of $Ti_3C_2T_x$ MXene thin film spray coated for 60 min on FTO coated glass substrate, b) TEM image showing the flake like morphology, c) HRTEM image with d spacing analysis, and d) SAED pattern, of $Ti_3C_2T_x$ MXene thin film spray coated for 60 min on a polymer substrate.

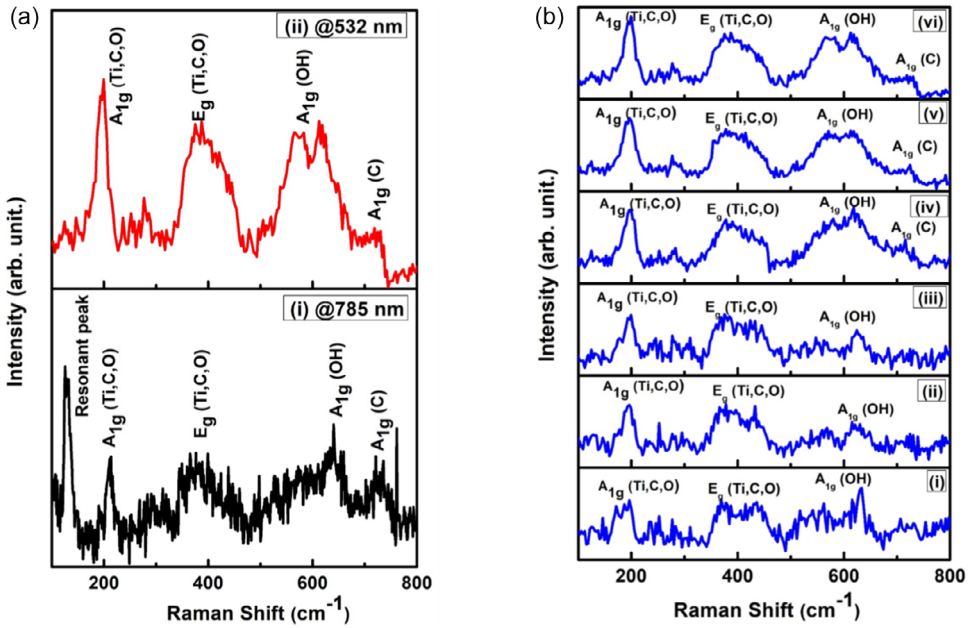

Figure 7. a) Raman spectra of $Ti_3C_2T_x$ MXene thin film deposited on a polymer substrate for a spray time of 60 min using an excitation wavelength of (i) 785 nm and (ii) 532 nm laser wavelength. b) Raman Spectra of $Ti_3C_2T_x$ MXene thin films using an excitation wavelength of 532 nm for $Ti_3C_2T_x$ MXene thin films deposited at different spray times (i) 10 min, (ii) 20 min, (iii) 30 min, (iv) 40 min, (v) 50 min, and (vi) 60 min.

a similar behavior (Figure S2b in Supporting Information). The A_{1g} and E_g mode associated with titanium, carbon, and oxygen atoms was obtained using an excitation of 532 nm. The A_{1g} modes are symmetrical stretching vibrations that are sensitive to the arrangement and size of the flakes in MXene.[68] An increase in intensity for A_{1g} peak with spray time suggests a higher degree of ordering and possibly larger flake sizes within the MXene structure.[69] The presence of a peak at around 600 cm^{-1} indicates A_{1g} vibrations involving hydroxyl groups.[70] The A_{1g}(C) mode, identifiable at 720 cm^{-1}, represents carbon vibrations. The increased intensity of the A_{1g}(Ti, C, O) mode, as well as the A_{1g}(C) mode, with longer spray time (Figure 7b), indicates an increase in the $Ti_3C_2T_x$ MXene flake size with spray time giving sharper Raman signals.

The spectra taken with 785 nm excitation show similar peaks, albeit with a notable resonant peak at 120 cm^{-1}, coupled with the plasmonic peak, corresponding to an interband transition at 1.6 eV.[69,71] This transition results in a broad peak in the UV-vis spectra of $Ti_3C_2T_x$ 785 nm. Figure S5 of Supporting Information shows the UV-Vis NIR spectra of the thin film deposited at various spray times, showing a plasmonic peak around 785 nm (a dip in transmission spectra). The UV-Vis NIR spectra also indicate a tunability of optical transmittance of the $Ti_3C_2T_x$ thin film from 50 to 6% with the increase in the thickness of the thin film. The resonance Raman phenomenon happens when the laser wavelength coincides or is marginally shorter than the transition wavelength. The 633 nm laser establishes conditions for resonance, though the ensuing peak strength is considerably reduced. At 785 nm excitation wavelength, the ratio of A_{1g}(C)/A_{1g}(Ti, C, O) is 0.9. A higher intensity of A_{1g}(Ti, C, O) peak indicates that this is due to the vibration of the flake as a whole, similar to that observed in TMDs.[69]

The survey spectrum (Figure S6, Supporting Information) of $Ti_3C_2T_x$ MXene thin film deposited for a spray time of 60 min on polymer substrate confirms the presence of Ti, C, O, and F. Notably, no detectable Al signal was observed, indicating the successful etching of the sample and effective removal of aluminum from the precursor material. The Ti 2p core level spectrum of $Ti_3C_2T_x$ MXene thin film deposited for a spray time of 60 min on polymer substrate is shown in **Figure 8**a. In the sample, Ti—C bound to =O or –OH functional groups appears at ≈455 eV, contributing to its hydrophilic nature.[72] The spectrum comprises two peaks at roughly 455 and 463 eV, corresponding to Ti $2p_{3/2}$ and Ti $2p_{1/2}$, respectively. The split is due to spin-orbit splitting, and both peaks contain information about the Ti bonding environment. Its deconvolution in a Gaussian function reveals the presence of Ti in multiple states, including Ti—(O/OH), Ti^{2+} –(O/OH), and Ti^{3+} –(O/OH), indicating different oxidation states and bonding environments.[73] The evaluation of the Ti 2p region also enables the identification of the extent of oxidation of the sample. The TiO_2 peak centered around 459 eV was less intense compared to Ti—(O/OH) and Ti^{2+} –(O/OH), indicating the sample is less oxidized. In the C1s region (Figure 8b), the peaks centered around 284 eV correspond to various carbon species. The deconvoluted peaks reveal contributions from C—Ti—(O/OH/F), C—C, and CH_x/C—O, illustrating the mixed bonding nature of carbon in the MXene. The C—Ti bond, a crucial indicator of the MXene's integrity, is accompanied by peaks corresponding to surface termination groups like hydroxyl and oxide, confirming the surface's functionalization. This functionalization can enhance the hydrophilicity of the MXene, affecting its interactions with other materials and its application performance. In the O 1s region (Figure 8c), the spectrum in the range of 529 to 533 eV shows peaks corresponding to TiO_2 and

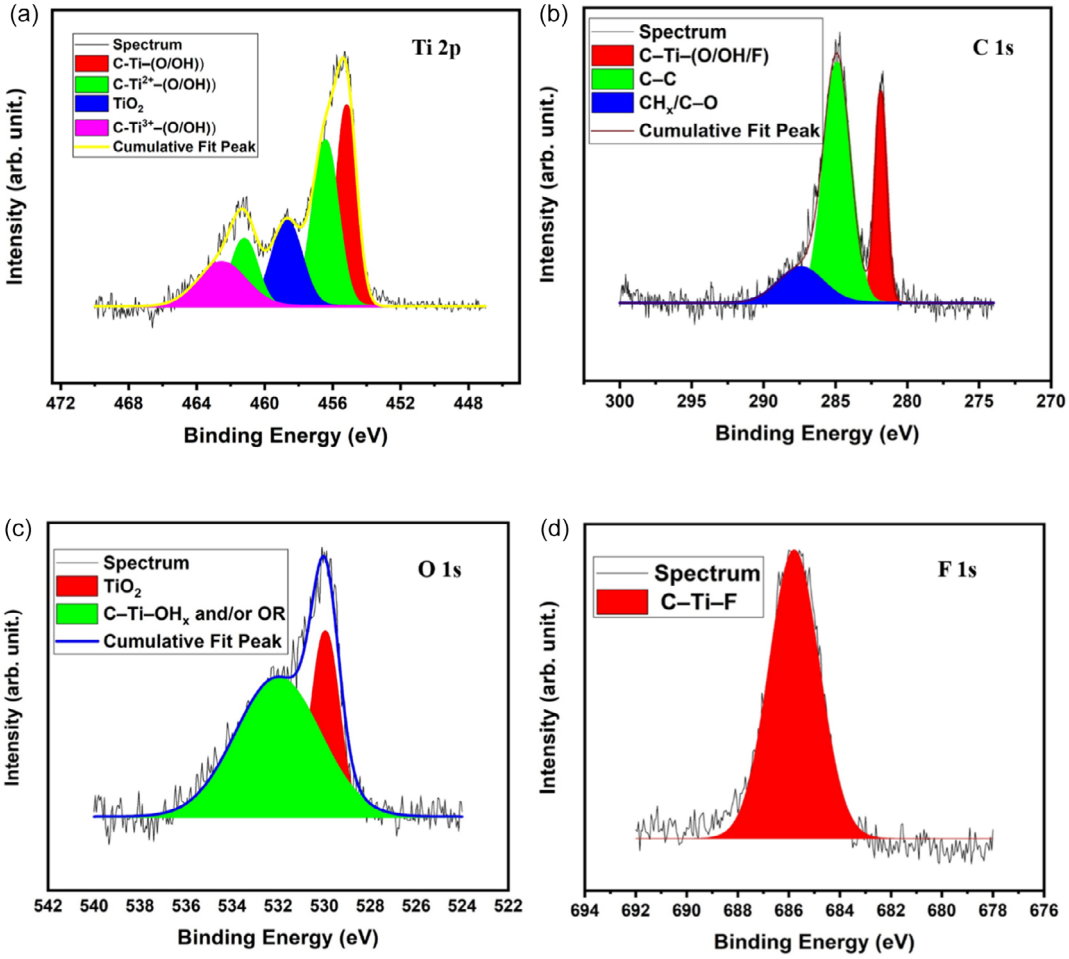

Figure 8. Component peak fitting of the XPS data of $Ti_3C_2T_x$ MXene thin film deposited for spray time 60 min on polymer substrate a) Ti 2p region, b) C 1s region, c) O 1s region, and d) F 1s region.

C–Ti–OH_x. This indicates the presence of oxide layers and hydroxyl groups on the MXene surface.[74] A distinct peak at ≈686 eV in the F 1s region (Figure 8d) is assigned to C—Ti—F, suggesting fluorine termination on the MXene surface. Fluorinated Al, C, or TiO_2 impurities were not traced in the F 1s spectrum. The absence of fluorinated impurities indicates that fluorine is primarily bonded to Ti in the MXene structure. This confirms successful surface functionalization without excessive fluorination or unwanted byproducts from the etching process.[72] Additionally, Figure S7 in Supporting Information presents the XPS spectra of $Ti_3C_2T_x$ MXene thin film deposited on a fluorine-doped tin oxide (FTO) substrate. This further supports the analysis of elemental composition and surface terminations across different substrates, demonstrating the reproducibility and stability of the MXene's chemical environment.

The electrical conductivity of the Ti_3AlC_2 MAX phase precursor was found to be 11.27 S m^{-1}. **Figure 9** shows the variation of the conductivity of the prepared $Ti_3C_2T_x$ MXene thin film with spray time. The conductivity of the thin film showed a gradual increase with spray time, varying from 1.31×10^4 S m^{-1} for the thin film prepared at 20 min to 2.32×10^4 S m^{-1} for the thin film prepared at 60 min. Apart from the sudden increase in conductivity at a spray time of 30 min, the further increase was slow, and the rate of increase of conductivity plateaus near 2.32×10^4 S m^{-1} at 60 min spray time. This may be due to the

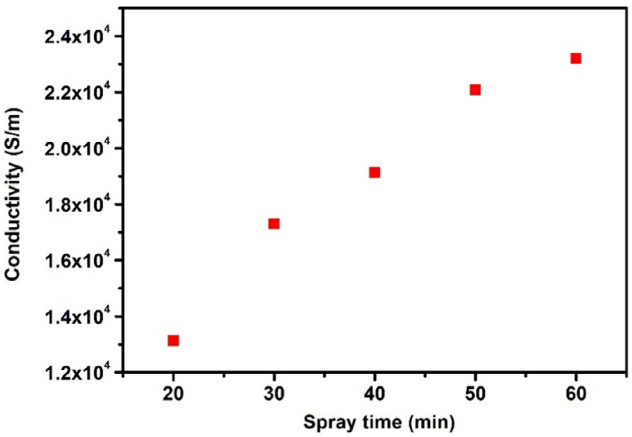

Figure 9. Variation of conductivity of $Ti_3C_2T_x$ MXene thin films deposited at different spray times.

formation of flakes of large size. The large flake size is believed to contribute to conductivity due to the reduction of scattering of charge carriers at grain boundaries. The larger flakes formed at longer spray times also contribute to the increased mass loading of the electrode. The variation in mass loading with spray time is given in Table S3 of the Supporting Information.

The electrochemical analysis of the thin films deposited at various spray times is given in **Figure 10**. The cyclic voltammetry (CV) (Figure 10a) exhibits well-defined redox peaks supporting the pseudocapacitive nature of the synthesized MXene thin films. The redox peaks are attributed to the oxidation and reduction of Ti^{3+} ions, respectively. When hydrogen ions intercalate, they protonate the oxygen functional group on the surface, forming a hydroxyl group. This process also alters the oxidation state of titanium, between +3 and +4, corresponding to the bonding and breaking of the oxygen functional group during anodic scan and cathodic scan as shown in Equations (6) and (7).[75]

$$Ti_3^{3+}C_2O_2 + 2H^+ = Ti_3^{4+}C_2OH + 2e^- \quad (6)$$

$$Ti_3^{4+}C_2OH + 2e^- = Ti_3^{3+}C_2O_2 + 2H^+ \quad (7)$$

The influence of spray time on the electrochemical behavior is apparent. As the spray time increases from 20 to 60 min, the area under the CV curves also increases, indicating an enhancement in capacitance. This trend is corroborated by the galvanostatic charge discharge (GCD) profiles (Figure 10b), where longer spray time results in longer charge–discharge times, reflecting higher capacitance. This improvement can be attributed to more extensive coverage of the active material, enhancing the conductivity and accessibility of electrolyte ions to the electrode surface and thus increasing the overall electrochemical activity. Improved electrical conductivity reduces charge transfer resistance, allowing for faster electron transport during redox reactions. This results in higher current densities and better capacitive performance. The areal capacitance values increase with spray time (Figure 10c), reaching a maximum of 41.93 mF cm^{-2} for the thin film deposited at a spray time of 60 min. At a lower scan rate of 5 mV s^{-1}, due to the enhanced ion diffusion and redox reaction kinetics within the electrode material, the areal capacitance increases to 62.15 mF cm^{-2} for the film deposited for 60 min.

The Nyquist plot (Figure 10d) provides insights into the charge transfer resistance (R_{ct}) and solution resistance (R_s) of thin films prepared at different spray times. The transmission line element (T) models the distributed resistive and capacitive effects in porous electrodes or systems with complex interfacial properties.[76] Thin films prepared at shorter times (20 and 30 min) exhibit larger semicircles, indicating higher R_{ct}, suggesting sluggish charge

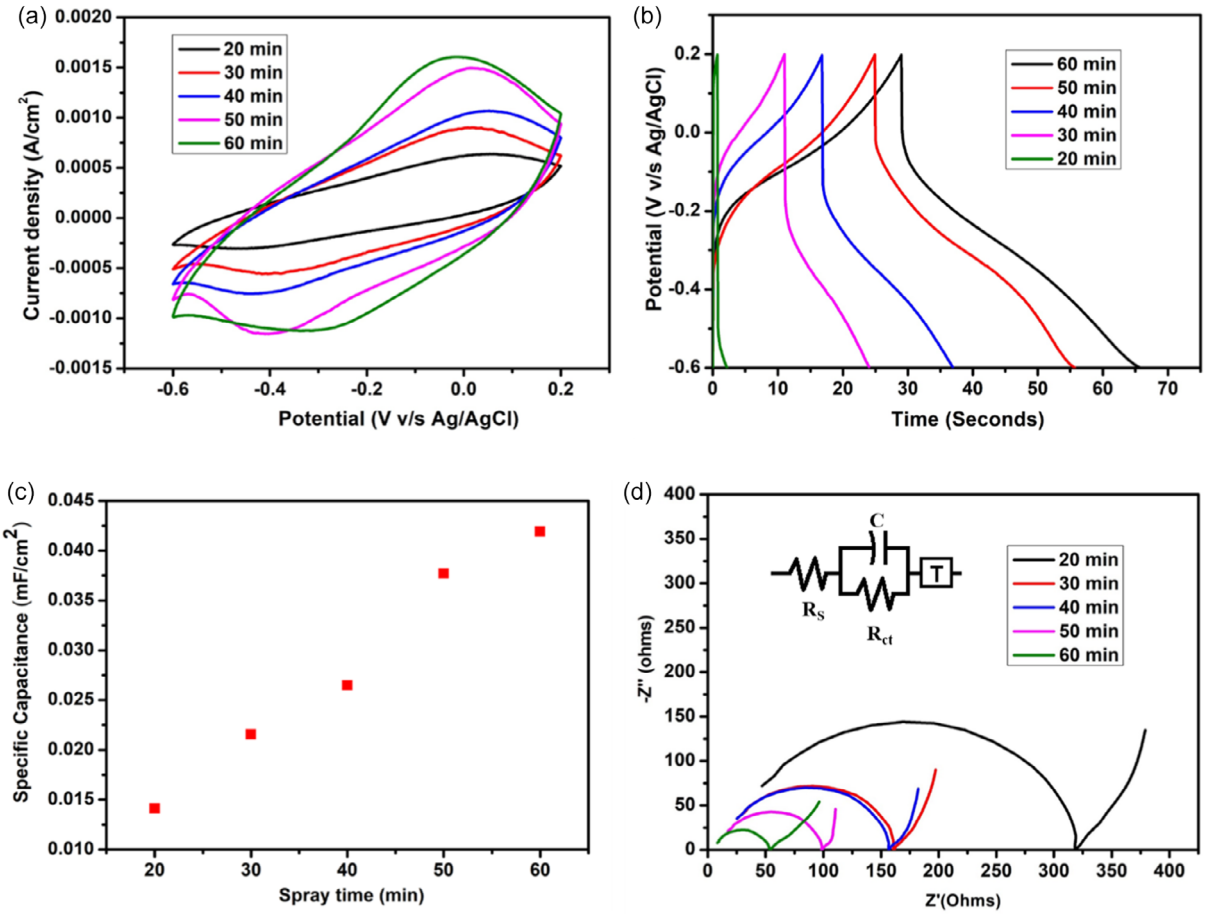

Figure 10. Electrochemical analysis of $Ti_3C_2T_x$ MXene thin films deposited at various spray times. a) CV at a scan rate of 20 mVs^{-1}. b) GCD at a current density of 0.9 mA cm^{-2}. c) Variation of areal capacitance with spray time. d) Nyquist plots with the inset showing the equivalent circuit.

transfer kinetics. As the time increases (40, 50, and 60 min), the diameter of the semicircles decreases, indicating a significant reduction in R_{ct} and improved charge transfer efficiency. The variation of solution resistance (R_s) and charge transfer resistance (R_{ct}) of the thin films with the spray duration is given in Table S4 of the Supporting Information. Thin film prepared at a spray time of 60 min had the highest areal capacitance and lowest values for equivalent series resistance (ESR) and equivalent parallel resistance (EPR) as 7.85 and 46.02 Ω respectively, suggesting that the spray time enhances the electrochemical activity of $Ti_3C_2T_x$ MXene thin films by optimizing its surface properties and reducing the barriers for electron transfer.

The CV of $Ti_3C_2T_x$ thin film deposited at 60 min spray time with various scan rates is given in **Figure 11**a. As the scan rate increases, redox peaks are not prominent in the CV, indicating capacitive behavior. The faster redox reactions at a higher scan rate limit the electrode–electrolyte interaction, reducing the prominence of redox peaks.[64] The GCD (Figure 11b) at different current densities also supports this observation; the IR drop becomes more pronounced at higher current densities, indicating increased resistance or slower charge transfer processes. The film showed a capacitance retention of nearly 90% after 5000 cycles (Figure 11c). The kinetics of CV can be assessed through an equation introduced by Dunn in 2007 to verify the pseudocapacitive characteristics:[77]

$$i(V) = k_1 v + k_2 v^{1/2} \tag{8}$$

Here, V represents the applied potential in volts, while v denotes the scan rate in Vs^{-1}. The parameters k_1 ($Acm^{-2}\,Vs^{-1}$) and k_2 ($Acm^{-2}\,V^{1/2}s^{-1/2}$) help to distinguish between capacitive-controlled and diffusion-controlled mechanisms, respectively. By plotting $v^{1/2}$ against $i(V)/v^{1/2}$, a linear relationship can be obtained, where the slope k_1 corresponds to the capacitive input, and the y-intercept k_2 represents the diffusion input. The linear relationship predicted by the equation was confirmed (as shown in **Figure 12**a). Additionally, this equation was employed to compute the capacitive contribution to the total current at varying scan rates, as depicted in Figure 12b. The capacitive contribution at a scan rate of 100 mVs^{-1} shows that the capacitive contribution increases with the scan rate, indicating a dominant capacitive behavior (Figure 12c). This equation can be simplified further to

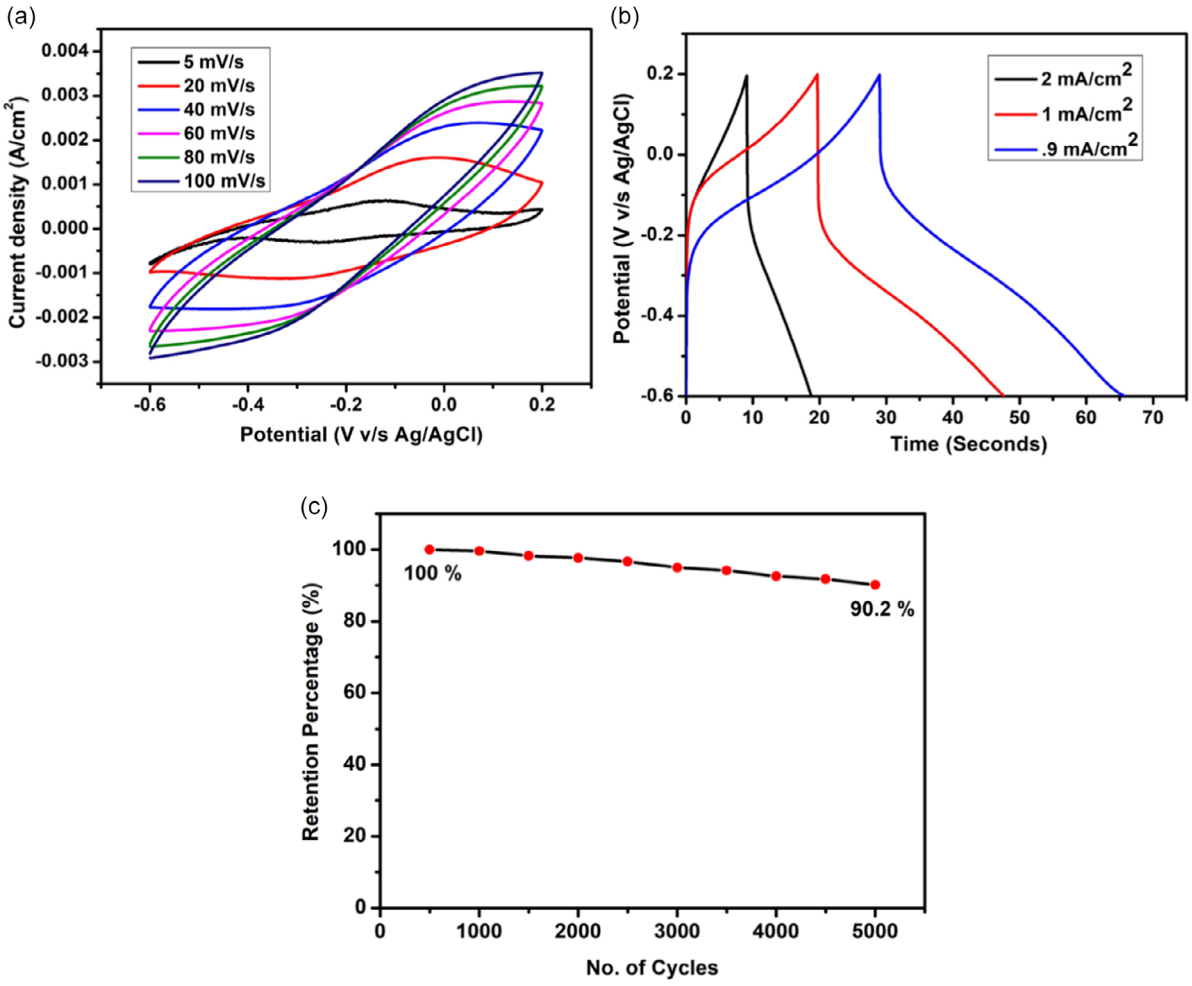

Figure 11. Electrochemical analysis of $Ti_3C_2T_x$ MXene thin film deposited a spray time of 60 min. a) CV recorded at different scan rates. b) GCD at different current densities. c) Capacitance retention with number of cycles.

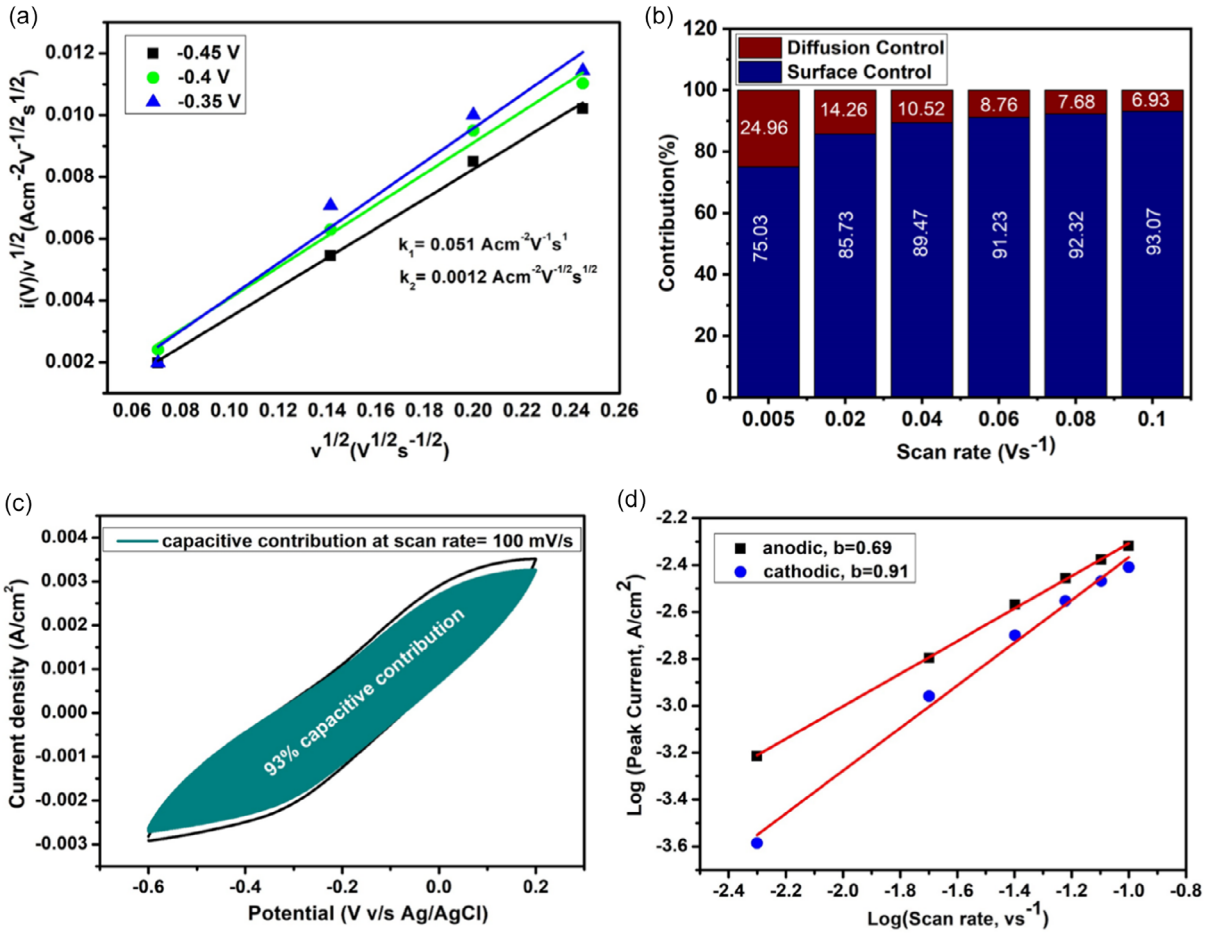

Figure 12. a) $i/\nu^{1/2}$ versus $\nu^{1/2}$ graphs at various potentials of $Ti_3C_2T_x$ MXene thin film deposited for a spray time of 60 min at various potentials. b) Fraction of capacitive and diffusion contribution. c) Fraction of capacitive contribution at 100 mVs^{-1} in the CV of $Ti_3C_2T_x$ MXene thin film deposited for a spray time of 60 min. d) Log(i) versus Log(v) plot.

$$i(V) = a\nu^b \tag{9}$$

In this context, the exponent b can be determined from the slope of the log (peak current) against the log (scan rate) plot. A b value approaching 1 implies surface-governed capacitive reactions, whereas a b value close to 0.5 signifies diffusion-driven reactions.[64] Analysis of the anodic and cathodic peaks of thin film deposited for 60 min using this equation yielded b values of 0.69 and 0.91, respectively (as seen in Figure 12d), which further supports the predominance of surface-based capacitive processes. A comparison of the obtained areal capacitance of thin film with some of the recently published works is given in Table S1, Supporting Information.

Figure S8 in Supporting Information shows the impedance plots for the PVA-H_2SO_4-based GPE films with different molar concentrations of H_2SO_4. The GPE film with 0.5 M concentration of H_2SO_4 had an ionic conductivity of 10.2 mS cm^{-1}. It was used to fabricate a symmetric all-solid-state supercapacitor using the $Ti_3C_2T_x$ MXene thin films grown over flexible CC. The $Ti_3C_2T_x$ MXene thin films were spray coated onto CC for a spray time of 60 min, a condition that gave the maximum areal capacitance on polymer substrates. **Figure 13**a,b illustrates the CV and GCD curves, respectively, of the all-solid-state symmetric device. The equivalent circuit used to fit the Nyquist plot is shown in the inset of Figure 13c. This circuit comprises the equivalent series resistance (R_s), charge transfer resistance (R_{ct}), capacitive element (C), and Warburg diffusion element (W). The intercept of the plot with the x-axis indicates the value of R_s, which is found to be 0.27 Ω. The absence of a semicircular region on the high-frequency side of the Nyquist plot indicates a very small charge transfer resistance. The device shows more than 87% capacitance retention after 5000 cycles (Figure 13d). The device achieved an areal capacitance of 28.40 mF cm^{-2}, an energy density of 2.52 μWh cm^{-2}, and a power density of 105.20 μW cm^{-2} at a current density of 1 mA cm^{-2}. A comparison of the obtained energy density and power density with some of the recently published works is given in Table S2, Supporting Information.

The mechanism for the increase in areal capacitance with spray time can be proposed considering the structural and morphological evolution of the thin films with spray time. The size of $Ti_3C_2T_x$ MXene flakes is found to increase with the spray time according to the FESEM image (Figure 5). The small and densely packed flakes grow larger and more defined with spray duration.

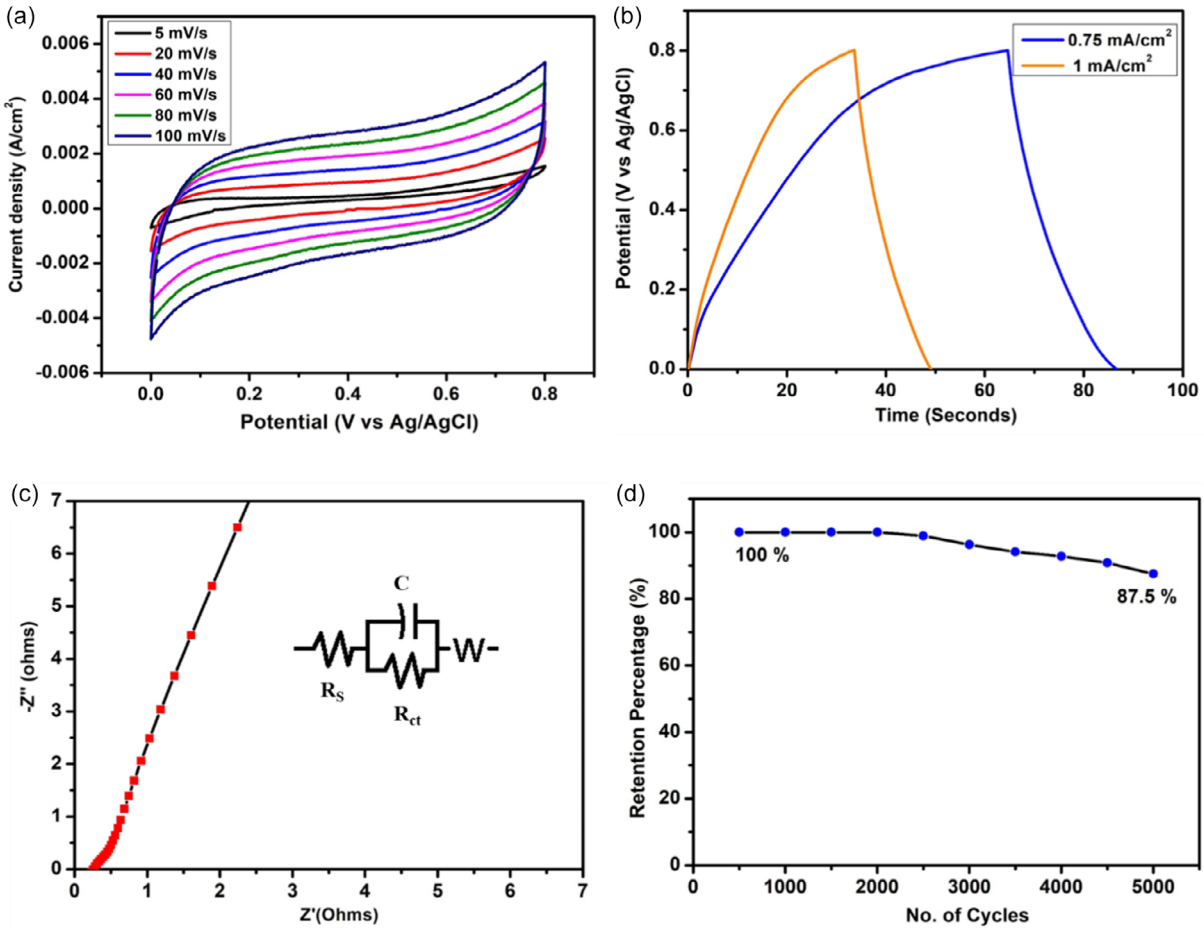

Figure 13. The electrochemical analysis of all solid state symmetric device using CC/$Ti_3C_2T_x$ MXene as the electrode. a) CV at various scan rates. b) GCD at a current density of 1 mA cm^{-2}. c) Nyquist plot of symmetric device. d) Capacitance retention with number of cycles.

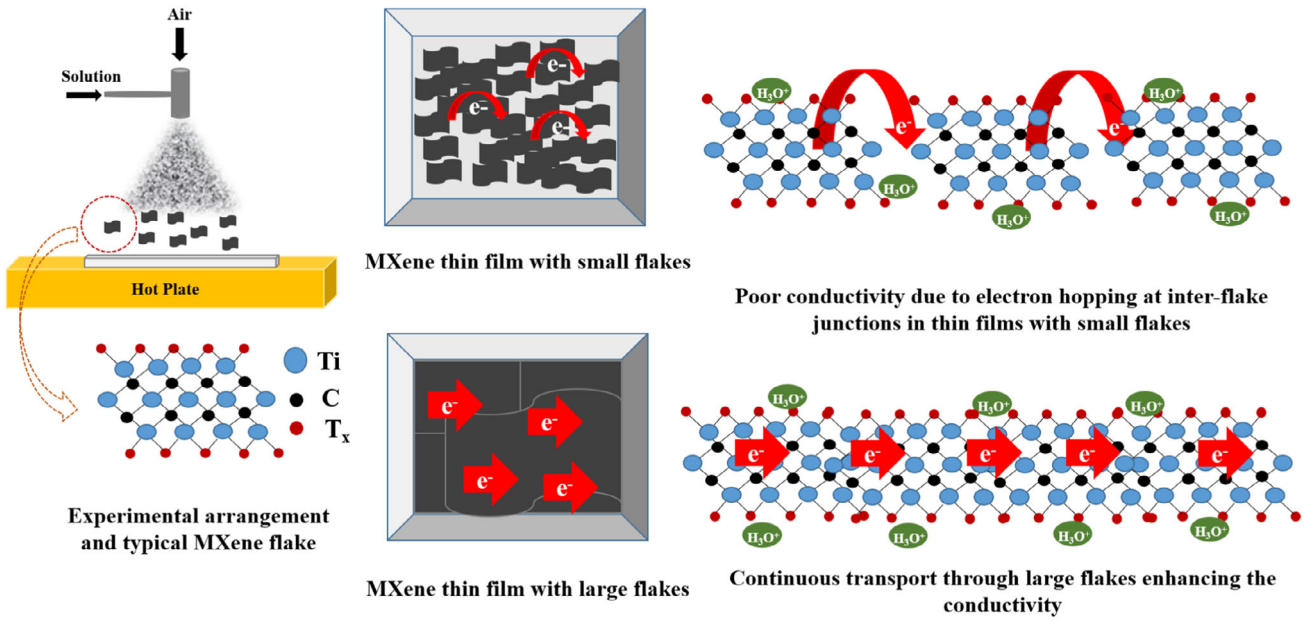

Figure 14. Schematic illustration of the mechanism of electron transport through small and large $Ti_3C_2T_x$ MXene flakes.

The XRD patterns reveal a significant increase in the intensity of the (002) peak with longer spray time. The (002) peak corresponds to the d-spacing between $Ti_3C_2T_x$ layers, and an increase in its intensity suggests that the flakes are stacking more effectively, leading to a better alignment and more efficient electron transport. Also, the increased interlayer spacing allows for easier ion diffusion, which is critical for enhanced electrochemical performance in energy storage applications. Further, the Raman spectra showed clear evidence of the formation of large flake sizes with spray duration, with the increase in the intensity of A_{1g} (Ti, C, O) and A_{1g} (C) peaks. The correlation between structural and morphological properties with the spray time helps in proposing a mechanism for the increase in conductivity and hence electrochemical response with spray time, as given in **Figure 14**. For small $Ti_3C_2T_x$ flakes, the electron transport is hindered by numerous inter-flake junctions, leading to increased resistance. The growth in flake size leads to a reduction in inter-flake junctions, typically sites of increased resistance. The larger flakes create more uniform pathways for electron transport, thereby enhancing conductivity. Also, the larger interlayer spacing associated with these networks aids in electron transport and provides channels for ion transport, which is essential for high-rate electrochemical processes. The Ragone plot showing comparison of energy density and power density of the fabricated device with other recently published works is shown in Figure S9, Supporting Information. The cycling stability of the synthesized thin film as well as the fabricated symmetric device was tested, and both showed a stable performance as indicated by the CV and GCD of the first cycle as well as the 5000th cycle (Figure S10, Supporting Information).

4. Summary and Conclusion

The study demonstrates the scalable fabrication of $Ti_3C_2T_x$ MXene films on flexible substrates via spray coating, achieving precise control over thickness and transparency. The thin films showed an interlayer spacing of 1.5 nm, optical transmittance of 50–6%, and conductivity of $2.32 \times 10^4\,S\,m^{-1}$, yielding an areal capacitance of $62.15\,mF\,cm^{-2}$ at $5\,mV\,s^{-1}$. Morphological and structural analyses revealed well-aligned flakes with minimal junctions, enabling excellent electron transport and structural integrity. A symmetric supercapacitor using PVA-H_2SO_4 gel electrolyte having an ionic conductivity of $10.2\,mS\,cm^{-1}$ and $Ti_3C_2T_x$ MXene films on CC as electrodes exhibited an areal capacitance of $28.40\,mF\,cm^{-2}$, energy density of $2.52\,\mu Wh\,cm^{-2}$, and power density of $105.20\,\mu W\,cm^{-12}$. This work highlights $Ti_3C_2T_x$ MXene films as promising electrode materials for flexible, high-performance thin film supercapacitors for powering wearable devices.

Acknowledgements

V.V. acknowledges CUSAT for UJRF. The authors acknowledge RUSA 2.0 and UGC CSR for financial assistance, RUSA CUSATECH for the faculty exchange program, and Spanish Ministry of Science and Innovation/AEI under Project PID2020-114796RB-(PROYECTO/AEI/10.13039/501100011033), MFA 2022/009 (SPINOD), and TED2021-132656B-C22, as well as to the Generalitat Valenciana (Conselleria d'Educació, Universitats i Ocupació) under Project PROMETEU/2021/066 and Prometeu/2021/082. The authors would also like to acknowledge access to the Servei Central de Suport a la Investigació Experimental (SCSIE) of the University of Valencia.

Conflict of Interest

The authors declare no conflict of interest.

Data Availability Statement

The data supporting this article have been included as part of the Supporting Information.

Keywords

flexible, spray coating, supercapacitors, thin film, $Ti_3C_2T_x$ MXene, wearable electronic devices

Received: February 18, 2025
Revised: June 4, 2025
Published online:

[1] Z. Yan, S. Luo, Q. Li, Z. S. Wu, S. Liu, *Adv. Sci.* **2024**, *11*, 1.
[2] N. Kumar, S. Bin Kim, S. Y. Lee, S. J. Park, *Nanomaterials* **2022**, *12*, 3708 HYPERLINK.
[3] S. Iravani, R. S. Varma, *Mater. Adv.* **2023**, *4*, 4317.
[4] J. Ma, Z. Cui, Y. Du, J. Zhang, C. Sun, C. Hou, N. Zhu, *Adv. Fiber Mater.* **2022**, *4*, 1535.
[5] Y. Wang, X. Wang, X. Li, X. Li, Y. Liu, Y. Bai, H. Xiao, G. Yuan, *Adv. Funct. Mater.* **2021**, *31*, 1.
[6] P. Lamba, P. Singh, P. Singh, P. Singh, Bharti, A. Kumar, M. Gupta, Y. Kumar, *J. Energy Storage* **2022**, *48*, 103871.
[7] D. Khalafallah, M. A. Ibrahim, H. Hou, J. Wang, C. Liu, Q. Zhang, *Sustainable Mater. Technol.* **2025**, *43*, e01286.
[8] D. Khalafallah, Q. Zhang, *Nano Mater. Sci.* **2025**, https://doi.org/10.1016/j.nanoms.2025.01.002.
[9] D. Khalafallah, N. Ibrahim, L. Mohammed, Q. Zhang, *Carbon* **2025**, *231*, 119683.
[10] D. Khalafallah, Q. Zhang, *J. Energy Storage* **2024**, *95*, 112621.
[11] D. Khalafallah, Y. Zhang, H. Dai, C. Liu, Z. Qinfang, *Carbon* **2024**, *227*, 119250.
[12] D. Khalafallah, N. Ibrahim, W. Cao, D. Song, J. Wang, Q. Zhang, *J. Energy Storage* **2025**, *110*, 115343.
[13] D. Khalafallah, Y. Zhang, Q. Zhang, *Batteries Supercaps*, **2024**, *8*, e202400497.
[14] D. Khalafallah, W. Huang, M. Zhi, Z. Hong, *Energy Environ. Mater.* **2024**, *7*, e12528.
[15] D. Khalafallah, W. Huang, M. Wunn, M. Zhi, Z. Hong, *J. Energy Storage* **2022**, *45*, 103716.
[16] P. Bhojane, *J. Energy Storage* **2022**, *45*, 103654.
[17] Y. Gogotsi, R. M. Penner, *ACS Nano* **2018**, *12*, 2081.
[18] H. Qian, A. R. Kucernak, E. S. Greenhalgh, A. Bismarck, M. S. P. Shaffer, *ICCM Int. Conf. Compos. Mater.* **2013**, *2013*, 2238.
[19] I. I. Gurten Inal, Z. Aktas, *Appl. Surf. Sci.* **2020**, *514*, 145895.
[20] L. F. Aval, M. Ghoranneviss, G. B. Pour, *Heliyon* **2018**, *4*, e00862.
[21] R. Liang, Y. Du, P. Xiao, J. Cheng, S. Yuan, Y. Chen, J. Yuan, J. Chen, *Nanomaterials* **2021**, *11*, 1248.
[22] X. Li, D. Du, Y. Zhang, W. Xing, Q. Xue, Z. Yan, *J. Mater. Chem. A. Mater.* **2017**, *5*, 15460.

[23] S. Zhang, J. Liu, L. Wang, Z. Zhang, J. Kang, P. Liu, W. Wang, *Chem. Eng. J.* **2021**, *405*, 126632.
[24] W. Wang, J. Cao, J. Yu, F. Tian, X. Luo, Y. Hao, J. Huang, F. Wang, W. Zhou, J. Xu, X. Liu, H. Yang, *Polymers* **2023**, *15*, 1856.
[25] S. Mahala, K. Khosravinia, A. Kiani, *J. Energy Storage* **2023**, *67*, 107558.
[26] B. S. Harisha, B. Akkinepally, J. Shim, J. Lim, *Chem. Eng. J.* **2025**, *508*, 160207.
[27] H. P. Hayat, F. K. Dokan, M. S. Onses, E. Yılmaz, A. Duran, E. Sahmetlioglu, *Mater. Res. Bull.* **2024**, *175*, 112747.
[28] H. Peçenek, S. Yetiman, F. K. Dokan, M. S. Onses, E. Yılmaz, E. Sahmetlioglu, *Ceram. Int.* **2022**, *48*, 7253.
[29] S. Alipoori, S. Mazinani, S. H. Aboutalebi, F. Sharif, *J. Energy Storage* **2020**, *27*, 101072.
[30] X. Wang, Y. Li, F. Lou, M. E. Melandsø Buan, E. Sheridan, D. Chen, *RSC Adv.* **2017**, *7*, 23859.
[31] M. R. Lukatskaya, O. Mashtalir, C. Ren, Dall'agnese Y, P. Rozier, P. Taberna, M. Naguib, P. Simon, M. Barsoum, Y. Gogotsi, *Science* **2013**, *341*, 6153.
[32] J. Huang, Y. Hu, J. Li, H. Wang, T. Wang, H. Wu, Y. Li, M. Wang, J. Zhang, *ACS Energy Lett.* **2023**, *8*, 2316.
[33] A. B. Samui, P. Sivaraman, *Polymer Electrolytes: Woodhead Publishing Series in Electronic and Optical Materials*, C. Sequeira and D. Santos, Eds., Woodhead Publishing, **2010**, pp. 431–470.
[34] G. D'Altri, L. Yeasmin, V. Di Matteo, S. Scurti, A. Giovagnoli, M. Di Filippo, I. Gualandi, M. Cassani, D. Caretti, S. Panzavolta, E. Scavetta, M. Rea, B. Ballarin, *ACS Omega* **2024**, *9*, 6391.
[35] B. Jinisha, K. M. Anilkumar, M. Manoj, C. M. Ashraf, V. S. Pradeep, S. Jayalekshmi, *J. Solid State Electrochem.* **2019**, *23*, 3343.
[36] T. T. T. Vuong, H. Phan, N. Vu Thi Thu, P. Nguyen, H. Nguyen, H. Le, N. Nguyen, T. Phung, P. Le, *ACS Omega* **2024**, *9*, 27710.
[37] A. Thakur, S. N. K. Davidson, A. Bedford, H. Fang, Y. Im, V. Kanduri, B. Wyatt, S. Nemani, **2023**, *7*, 23000301.
[38] M. Hu, T. Hu, Z. Li, Y. Yang, R. Cheng, J. Yang, C. Cui, X. Wang, *ACS Nano.* **2018**, *12*, 3578.
[39] R. Garg, A. Agarwal, M. Agarwal, *Mater. Res. Express* **2020**, *7*, 22001.
[40] A. Shayesteh, S. Mirkhani, P. Sun, M. Naguib, P. Braun, U. Sundararaj, *Nanoscale* **2021**, *13*, 3572.
[41] A. C. Y. Yuen, T. Chen, B. Lin, W. Yang, I. Kabir, I. De Cachinho Cordeiro, A. Whitten, J. Mata, B. Yu, H. Lu, G. Yeoh, *Compos. Part C: Open Access* **2021**, *5*, 100155.
[42] C. Rong, T. Su, Z. Li, T. Chu, M. Zhu, Y. Yan, B. Zhang, F. Xuan, *Nat. Commun.* **2024**, *15*, 1566.
[43] L. Liu, H. Zschiesche, M. Antonietti, B. Daffos, N. Tarakina, M. Gibilaro, P. Chamelot, L. Massot, B. Duployer, P. Taberna, P. Simon, *Adv. Energy Mater.* **2023**, *13*, 2202709.
[44] H. An, T. Habib, S. Shah, H. Gao, M. Radovic, M. Green, J. Lutkenhaus, *Sci. Adv.* **2018**, *4*, 6.
[45] Y. Zhou, L. Yin, S. Xiang, S. Yu, H. Johnson, S. Wang, J. Yin, J. Zhao, Y. Luo, P. Chu, *Adv. Sci.* **2024**, *11*, 1.
[46] C. Manjunatha, K. P. Shwetha, Y. Athreya, S. G. Kumar, M. K. S. Kamath, *ECS Sens. Plus* **2023**, *2*, 017002.
[47] S. V. Prabhakar Vattikuti, J. Shim, P. Rosaiah, A. Mauger, C. M. Julien, *Nanomaterials* **2024**, *14*, 62.
[48] X. Liu, Q. Fu, Z. Li, H. Wang, J. Ren, *Diam. Relat. Mater.* **2023**, *140*, 110474.
[49] K. L. Chai, M. M. Aung, I. M. Noor, H. N. Lim, L. C. Abdullah, *Sci. Rep.* **2022**, *12*, 124.
[50] K. R. G. Lim, M. Shekhirev, B. C. Wyatt, B. Anasori, Y. Gogotsi, Z. W. Seh, *Nat. Synth.* **2022**, *1*, 601.
[51] Y. Zhou, K. Maleski, B. Anasori, J. Thostenson, Y. Pang, Y. Feng, K. Zeng, C. Parker, S. Zauscher, Y. Gogotsi, J. Glass, C. Cao, *ACS Nano.* **2020**, *14*, 3576.
[52] I. Shaheen, B. Akkinepally, I. Hussain, S. Hussain, P. Rosaiah, A. Qureshi, J. Niazi, *J. Energy Storage* **2024**, *87*, 111513.
[53] X. Pu, M. Liu, L. Li, S. Han, X. Li, C. Jiang, C. Du, J. Luo, W. Hu, Z. Wang, *Adv. Energy Mater* **2016**, *6*, 1601254.
[54] R. Tao, Y. Gu, Z. Du, X. Lyu, J. Li, *Nat. Rev. Clean Technol.* **2025**, *1*, 116.
[55] Y. Cai, X. Chen, Y. Xu, Y. Zhang, H. Liu, H. Zhang, J. Tang, *Carbon Energy* **2024**, *6*, e501.
[56] M. Zhang, Y. Wang, F. Gao, Y. Wang, X. Shen, N. He, J. Zhu, Y. Chen, X. Wan, X. Lian, E. Hu, J. Xu, Y. Tong, *Ceram. Int.* **2019**, *45*, 19467.
[57] Md. Sharifuzzaman, S. Barman, M. Zahed, S. Sharma, H. Yoon, J. Nah, H. Kim, J. Park, *Small* **2020**, *16*, 2002517.
[58] J. Halim, M. Lukatskaya, K. Cook, J. Lu, C. Smith, L. Näslund, S. May, L. Hultman, Y. Gogotsi, P. Eklund, M. Barsoum, *Chem. Mater.* **2014**, *26*, 2374.
[59] Y. Li, B. Zhou, Y. Shen, C. He, B. Wang, C. Liu, Y. Feng, C. Shen, *Compos. B Eng.* **2021**, *217*, 108902.
[60] R. Tomov, V. Strijkova, V. Katrova, M. Aleksandrova, 2024 33rd *International Scientific Conference Electronics, ET 2024 - Proceedings*, Institute of Electrical and Electronics Engineers Inc., **2024**, https://doi.org/10.1109/ET63133.2024.10721495.
[61] S. Abdolhosseinzadeh, X. Jiang, H. Zhang, J. Qiu, C. (John) Zhang, *Mater. Today* **2021**, *48*, 214.
[62] K. Hantanasirisakul, M. Zhao, P. Urbankowski, J. Halim, B. Anasori, S. Kota, C. Ren, M. Barsoum, Y. Gogotsi, *Adv Electron Mater* **2016**, *2*, 1.
[63] A. Ali, A. Belaidi, S. Ali, M. I. Helal, K. A. Mahmoud, *J. Mater. Sci.: Mater. Electron.* **2016**, *27*, 5440.
[64] A. Ashok, T. K. Krishnapriya, S. B. Saseendran, M. K. Wilson, M. Niranjana, A. S. Asha, *Energy Technol.* **2023**, *11*, 1.
[65] A. Ashok, S. B. Saseendran, A. S. Asha, *Phys. Scr.* **2022**, *97*, 25807.
[66] M. Bandpey, D. P. J. Barz, *Nanoscale*, **2024**, *16*, 15078.
[67] L. Verger, V. Natu, M. Carey, M. W. Barsoum, *Trends Chem.* **2019**, *1*, 656.
[68] S. Adomaviciute-Grabusove, A. Popov, S. Ramanavicius, V. Sablinskas, K. Shevchuk, O. Gogotsi, I. Baginskiy, Y. Gogotsi, A. Ramanavicius, *ACS Nano.* **2024**, *18*, 13184.
[69] A. Sarycheva, Y. Gogotsi, *Chem. Mater.* **2020**, *32*, 3480.
[70] E. Berger, Z. P. Lv, H. P. Komsa, *J. Mater. Chem. C Mater.* **2022**, *11*, 1311.
[71] J. El-Demellawi, S. Lopatin, J. Yin, O. Mohammed, H. Alshareef, *ACS Nano.* **2018**, *12*, 8485.
[72] J. Halim, K. Cook, M. Naguib, P. Eklund, Y. Gogotsi, J. Rosen, M. Barsoum, *Appl. Surf. Sci.* **2016**, *362*, 406.
[73] V. Natu, M. Benchakar, C. Canaff, A. Habrioux, S. Célérier, M. W. Barsoum, *Matter* **2021**, *4*, 1224.
[74] R. Lotfi, M. Naguib, D. E. Yilmaz, J. Nanda, A. C. T. Van Duin, *J. Mater. Chem. A Mater.* **2018**, *6*, 12733.
[75] X. Zang, J. Wang, Y. Qin, T. Wang, C. He, Q. Shao, H. Zhu, N. Cao, *Nanomicro Lett.* **2020**, *12*, 1.
[76] A. Lasia, *J. Electroanal. Chem.* **1995**, *397*, 27.
[77] C. Choi, D. Ashby, D. Butts, R. DeBlock, Q. Wei, J. Lau, B. Dunn, *Nat. Rev. Mater.* **2020**, *5*, 5.